

RESOLVING THE FU ORI SYSTEM WITH ALMA: INTERACTING TWIN DISKS?

SEBASTIÁN PÉREZ,^{1,2} ANTONIO HALES,^{3,4} HAUYU BAOBAB LIU,⁵ ZHAOHUAN ZHU,⁶ SIMON CASASSUS,² JONATHAN WILLIAMS,⁷
ALICE ZURLO,^{8,9} NICOLÁS CUELLO,^{10,11} LUCAS CIEZA,⁸ AND DAVID PRINCIPE¹²¹Universidad de Santiago de Chile, Av. Libertador Bernardo O'Higgins 3363, Estación Central, Santiago²Departamento de Astronomía, Universidad de Chile, Casilla 36-D, Santiago³National Radio Astronomy Observatory, 520 Edgemont Road, Charlottesville, VA 22903-2475.⁴Joint ALMA Observatory, Alonso de Córdova 3107, Vitacura 763-0355, Santiago⁵Academia Sinica Institute of Astronomy and Astrophysics, P.O. Box 23-141, Taipei 10617, Taiwan⁶Department of Physics and Astronomy, University of Nevada, Las Vegas, 4505 S. Maryland Pkwy, Las Vegas, NV 89154, USA⁷Institute for Astronomy, University of Hawaii, Honolulu, HI 96822, USA⁸Núcleo de Astronomía, Facultad de Ingeniería y Ciencias, Universidad Diego Portales, Av. Ejercito 441, Santiago, Chile⁹Escuela de Ingeniería Industrial, Facultad de Ingeniería y Ciencias, Universidad Diego Portales, Av. Ejercito 441, Santiago, Chile¹⁰Instituto de Astrofísica, Pontificia Universidad Católica de Chile, Vicuña Mackenna 4860, 7820436 Macul, Santiago¹¹Núcleo Milenio de Formación Planetaria (NPF), Chile¹²Massachusetts Institute of Technology, Kavli Institute for Astrophysics, Cambridge, MA, USA

ABSTRACT

FU Orionis objects are low-mass pre-main sequence stars characterized by dramatic outbursts of several magnitudes in brightness. These outbursts are linked to episodic accretion events in which stars gain a significant portion of their mass. The physical processes behind these accretion events are not yet well understood. The archetypical FU Ori system, FU Orionis, is composed of two young stars with detected gas and dust emission. The continuum emitting regions have not been resolved until now. Here, we present 1.3 mm observations of the FU Ori binary system with ALMA. The disks are resolved at 40 mas resolution. Radiative transfer modeling shows that the emission from FU Ori north (primary) is consistent with a dust disk with a characteristic radius of ~ 11 au. The ratio between major and minor axes shows that the inclination of the disk is $\sim 37^\circ$. FU Ori south is consistent with a dust disk of similar inclination and size. Assuming the binary orbit shares the same inclination angle as the disks, the deprojected distance between north and south components is $0''.6$, i.e. ~ 250 au. Maps of ^{12}CO emission show a complex kinematic environment with signatures disk rotation at the location of the northern component, and also (to a lesser extent) for FU Ori south. The revised disk geometry allows us to update FU Ori accretion models (Zhu et al.), yielding a stellar mass and mass accretion rate of FU Ori north of $0.6 M_\odot$ and $3.8 \times 10^{-5} M_\odot \text{ yr}^{-1}$, respectively.

Keywords: accretion, accretion disks — stars: formation — individual: FU Ori

1. INTRODUCTION

Protostars build a significant fraction of their final mass through an accretion disk fed by a surrounding envelope. As this envelope dissipates, accretion rates tend to drop below 10^{-7} or even $10^{-8} M_\odot \text{ yr}^{-1}$. While most young stellar objects (YSOs) have luminosities that are significantly lower than expected from steady protostellar disk accretion (the so-called *luminosity problem*; Kenyon et al. 1990; Evans et al. 2009), some exhibit episodes of high activity, increasing their optical brightness by several orders of magnitude on time-scales as short as one year (see Audard et al. 2014, for a review). Accretion at this stage can reach up to $10^{-4} M_\odot \text{ yr}^{-1}$. A pos-

sible solution to the so-called luminosity problem is that most protostars also go through an ‘FUor’ (named after the class prototype FU Orionis) phase early in their life time. This would imply that a significant fraction of the mass of a young protostar is accreted in an episodic way, with prolonged periods of low accretion (Zhu et al. 2009; Vorobyov & Basu 2010; Bae et al. 2014).

An Early Science campaign to characterize FUor sources with the Atacama Large Millimeter/sub-millimeter Array (ALMA) shows that they are compact in radio continuum (Cieza et al. 2018). Their disk emission have smaller characteristic radii for a given disk mass than T Tauri disks and have disk sizes and masses that are more similar to those of Class I than to Class II sources (e.g., Sheehan & Eisner 2017; Tobin et al. 2018). FUors appear surrounded by prominent outflows of molecular gas with hourglass-like morphologies (e.g., V2775 Ori, Zurlo et al. 2017). These outflows can

sometimes display wide opening angles (e.g., HBC 494, Ruíz-Rodríguez et al. 2017a,b), and even show notable misalignments with respect to the orientation of the dust disk (e.g., V1647 Ori, Principe et al. 2018).

Episodic accretion and its implications for star and planet formation are not well understood. Several physical processes have been proposed to explain such dramatic accretion events. The most favored mechanisms include disk fragmentation and the subsequent inward migration of the fragments (Vorobyov & Basu 2010), gravitational instability (GI) and magneto-rotational instabilities (Armitage et al. 2001; Zhu et al. 2009, 2010; Martin & Lubow 2011; Bae et al. 2014), amongst others. These models predict the presence of distinct features (such as clumps and spiral arms) that should be detectable with current observational capabilities, although these have not been found on high resolution images of FUor disks (e.g. V883 Ori, Cieza et al. 2016).

Another possibility is that, since these young disks dwell in crowded star-forming regions, their outbursts may be connected to, or driven by, binary interactions (Bonnell & Bastien 1992; Reipurth & Aspin 2004), or star-disk flybys (e.g., Pfalzner 2008; Cuello et al. 2019) as stars are common and disks have large cross-sections, and possibly even disk-disk interactions (e.g., Muñoz et al. 2015). A few FUor-like protostars have now been identified as having binary components (e.g., L1551 IRS5, RNO 1B/C, AR 6A/B, Pueyo et al. 2012, and references therein), feeding the discussion on whether the rapid accretion could be caused by close-companion interactions. Perturbers such as planets have also been proposed as an explanation for the quick rise in the outburst lightcurves of FU Ori and V1057 Cyg (Clarke et al. 2005).

ALMA Early Science observations of the FU Ori binary system show that each binary component is surrounded by compact continuum emission (unresolved at $\sim 0''.6$ resolution) and widespread molecular emission (Hales et al. 2015). Using the Karl G. Jansky Very Large Array (JVLA) in its most extended configuration, Liu et al. (2017) separate the two binary disks, but the individual disks remain unresolved at 29 GHz with a $0''.07$ resolving beam. Combining these observations with lower (8-10 GHz) and higher frequency data, Liu et al. (2017) show that the 8 to 346 GHz SEDs of FU Ori North (or simply “FU Ori”, the primary) and FU Ori South (secondary) cannot be reproduced by constant spectral indices, suggesting a multi-component circumstellar environment (bearing in mind that these sources are time variable). Liu et al. (2017) also show that the observations can be explained by a circumstellar environment consisting of free-free emission from ionized gas, and thermal emission from two dust components, a compact optically thick disk and an optically thin region. On the other hand, Zhu et al. (2007) show that the optical-IR spectrum of FU Ori requires a hot disk with mass accretion of $2 \times 10^{-4} M_{\odot} \text{ yr}^{-1}$.

In this work, we present 40 mas resolution ALMA observations of the FU Ori system which resolve the continuum emitting regions around each stellar component, providing the first direct measure of their sizes at millimeter wavelengths

(Section 3). An analysis of the local kinematics around the FU Ori components using molecular line observations is presented in Section 4. Implications are discussed in Section 5, while Section 6 presents our concluding remarks. Throughout this work we use a distance to FU Ori of 416 ± 9 pc (Gaia Collaboration et al. 2018, DR2), consistent with the distance to the Orion Nebula Cluster from parallax of non-thermal radio emission (Menten et al. 2007).

2. OBSERVATIONS AND DATA REDUCTION

FU Ori was observed during ALMA Cycle 4 on September 6th 2017 using ALMA’s 12m array in extended (C40-8) configuration, with 42 antennas with baselines ranging from 41 m to 7.5 km. This configuration yields an angular resolution of $\sim 0''.05$ (~ 21 au) and a Maximum Recoverable Scale of $\sim 1''.05$ (~ 437 au) at 1.3 mm. The median precipitable water vapor column (PWV) was 0.35 mm, with clear sky conditions and an average phase RMS of 28.6° after WVR correction.

The primary flux calibrator was the quasar J0423–0120, while J0510+1800 was used as bandpass calibrator. The quasar J0532+0732, located 3.5° from the target was observed as phase calibrator, by alternating with the science target every 54 seconds to calibrate the time-dependent variation of the complex gains. The total time spent on-source was 39.8 minutes. A secondary phase calibrator (J0551+0829), located 4.7° from the phase calibrator, was observed regularly as a check source to assess the quality of the phase transfer. The ALMA correlator was configured in Frequency Division Mode (FDM). Two spectral windows with 1.875 GHz bandwidth were set up for detecting the dust continuum, centered at 232.005 GHz and 218.505 GHz, respectively. The $^{12}\text{CO}(2-1)$, $^{13}\text{CO}(2-1)$ and $\text{C}^{18}\text{O}(2-1)$ transitions of carbon monoxide were targeted by configuring three spectral windows at rest frequencies of 230.538 GHz, 220.399 GHz and 219.560 GHz respectively. The spectral resolution for the line observations was 122.070 kHz ($\sim 0.2 \text{ km s}^{-1}$). All data were calibrated by the ALMA staff using the ALMA Science Pipeline version r39732 in the CASA package (McMullin et al. 2007).

2.1. ALMA continuum imaging

Imaging of the 1.3 mm continuum emission was performed using the CLEAN task in CASA with uniform weighting, resulting in a synthesized beam size of 60×42 mas and position angle of 68.8° (Figure 1). Self-calibration of the data was performed to improve coherence. A single iteration of phase-only (i.e., no amplitude) calibration resulted in a 1.7 factor improvement in the resulting SNR ($30 \mu\text{Jy RMS}$) (compared to the SNR of a CLEAN image before self-calibration). Another iteration of self-calibration was found to improve only marginally the image quality.

As shown in Figure 1, both components of the FU Ori binary are detected in continuum emission, separated by $\sim 0''.5$. FU Ori north has a total flux density of 14.30 ± 1.5 mJy, while the southern component has a flux density of 7.94 ± 0.8 mJy (errors include the 10% uncertainty

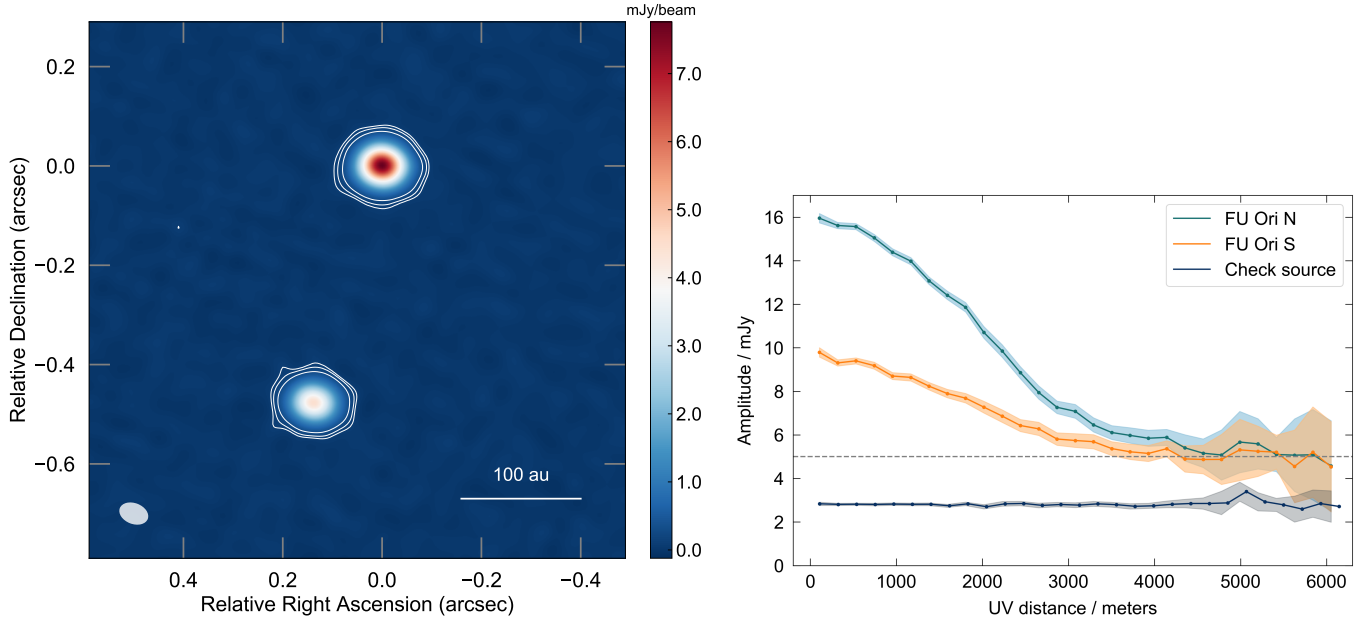


Figure 1. *Left:* 1.3 mm (225 GHz) continuum map of the FU Ori binary system. The image resolution is $0''.06 \times 0''.042$ (shown in left bottom corner). The contours are 3, 5, and 10 times the image RMS noise of $30 \mu\text{Jy beam}^{-1}$. North is up, East is left. *Right:* Visibility amplitude as a function of baseline lengths (UV distances) for FU Ori North (blue), FU Ori South (orange) and check source J0551+0829, with their respective uncertainties. The visibilities of both FU Ori components have a profile that decreases from the peak maximum to a 5 mJy floor level (dotted line). The signal for J0551+0829 is constant with baseline length, as expected for an unresolved source.

in the absolute flux calibration). The peak fluxes are 7.7 ± 0.8 and 4.4 ± 0.5 mJy beam $^{-1}$ for FU Ori north and south, respectively. The emitting regions around each component are resolved at 60×42 mas angular resolution. The deconvolved source sizes (as FWHM) measured using the CASA task `imfit` are $50.4 \pm 0.5 \times 39.9 \pm 0.6$ (mas) at position angle (PA) $133.6^\circ \pm 1.7^\circ$ and $47.7 \pm 0.8 \times 38.4 \pm 0.9$ (mas) at $137.7^\circ \pm 3.7^\circ$ for FU Ori N and FU Ori S, respectively. This corresponds to disk sizes of $7.5 \text{ au} \times 5.8 \text{ au}$ and $7.2 \text{ au} \times 5.7 \text{ au}$, north and south, respectively. The deconvolved sizes translate to an inclination angle of $37.7^\circ \pm 0.8^\circ$ and $36.4^\circ \pm 1.2^\circ$, for the north and south components, respectively. As will be shown in Section 4, the PA inferred from the continuum is in good agreement with rotation seen in the kinematics of FU Ori N.

As visibilities are spatially-integrated quantities, one of the components needs to be subtracted to inspect the visibilities of the other. This is achieved by subtracting the CLEAN model of one of the components from the visibility data. There are no indications of substructures in either disk, or of emission in between the stellar components in continuum. The observed visibilities of each component (right panels in Fig. 1) show the decreasing profile characteristic of extended sources (e.g. Wilson et al. 2009).

By imaging each continuum spectral window separately (218 and 232 GHz), we derive in-band spectral indices (using the full bandwidth of each spectral window, i.e., 1.875 GHz) of 2.1 for both FU Ori and FU Ori S. This is consistent with the spectral indexes derived in recent SED fitting (Liu et al. 2019). The ALMA data confirm both disks have almost iden-

tical spectral indices, consistent with the emission being optically thick.

2.2. ALMA ^{12}CO imaging

To construct channel maps of CO emission, a CLEAN procedure was performed on the continuum-subtracted data. We used a Briggs weighting scheme with a robust parameter of 1.0. This weighting yields the best results in terms of achieving good signal-to-noise without compromising on resolution. Channel maps were produced with a spectral resolution equivalent to 1 km s^{-1} . These broad channels are needed to pinpoint fast Keplerian kinematics as opposed to slow outflows. Each channel map has an RMS noise of $1.2 \text{ mJy beam}^{-1}$, for a CLEAN beam of $0''.1 \times 0''.09$. The 1σ noise level is 2 mJy beam^{-1} if systematics (large scale fringes in the central channels) are also included. (As shown in Hales et al. (2015), the kinematics is complex and it is heavily influenced by large scale cloud emission and absorption, and also possibly a slow outflow. A full analysis of the global kinematics, i.e., how outflowing and cloud material connect to the binary FU Ori kinematics, will be presented in a future publication (Hales et al. *in prep*). Here we focus on probing the kinematics of the gas in the vicinity of the FU Ori stars.

3. CONTINUUM MODELING

3.1. Radiative transfer

The radiative transfer (RT) modeling procedure described in Cieza et al. (2018) and Hales et al. (2018) is used to derive disk structural parameters. The model consists of a passively heated disk characterized by a power-law surface density pro-

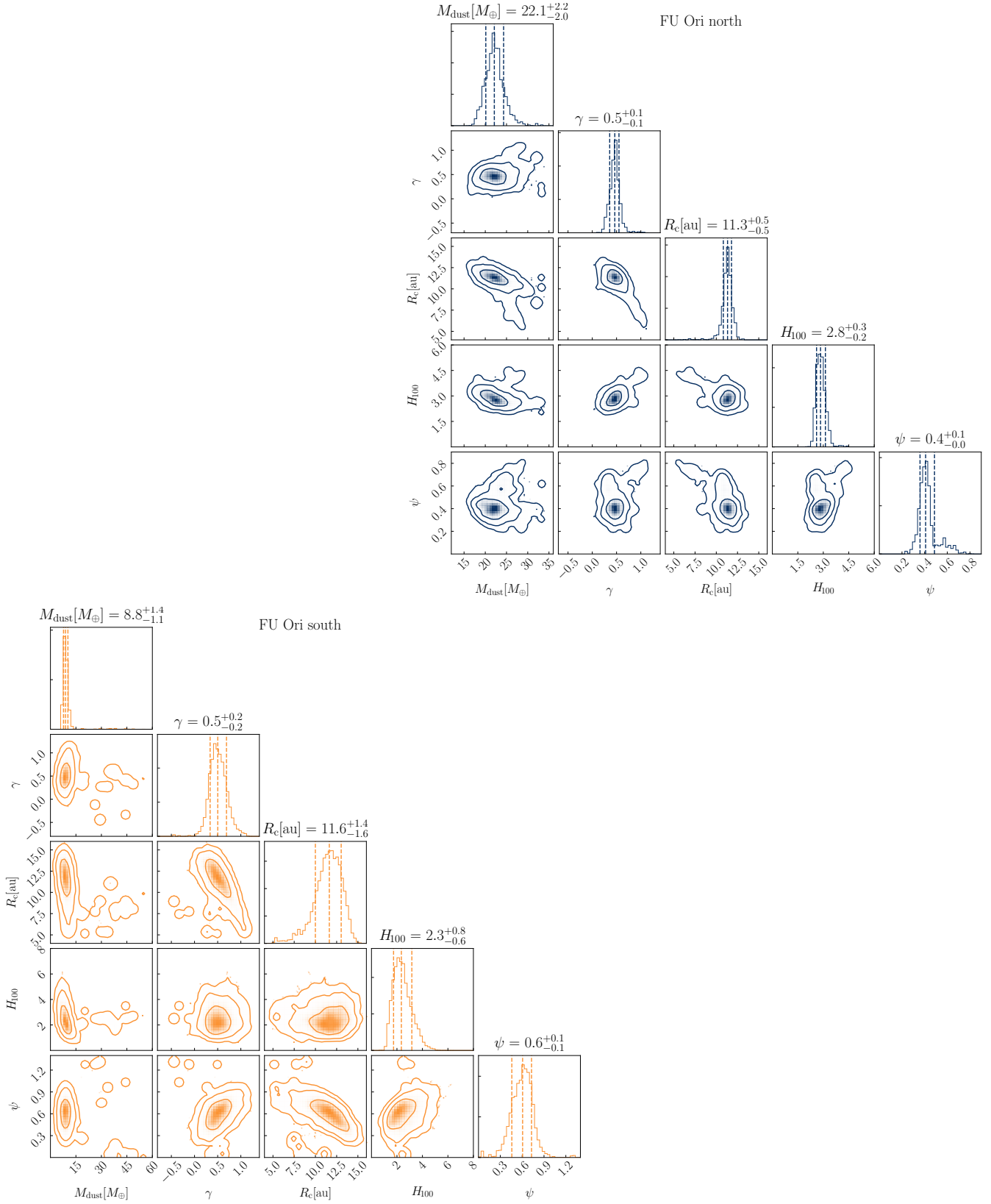


Figure 2. Posterior distributions of disk parameters M_{dust} , γ , R_c , H_{100} , and flaring index Ψ , including their marginalised distributions for FU Ori north (top right, blue) and south (bottom left, orange). The vertical dashed lines represent the 16th, 50th and 84th percentiles. Contours correspond to 68 per cent, 95 per cent and 99.7 per cent confidence regions. Units are specified on the panel titles. The plots were generated using the PYTHON module CORNER (Foreman-Mackey 2016).

file with slope γ and a *characteristic radius* R_c , defined by:

$$\Sigma(R) = \Sigma_c \left(\frac{R}{R_c} \right)^{-\gamma} \exp \left[- \left(\frac{R}{R_c} \right)^{2-\gamma} \right]. \quad (1)$$

The scale height as a function of radius is given by:

$$h(R) = h_c \left(\frac{R}{R_c} \right)^\Psi, \quad (2)$$

where h_c is the scale height at the characteristic radius R_c , and Ψ defines the degree of flaring in the disk. Here we use $H_{100} \equiv h(100 \text{ au})$ to enable comparison with previous modeling of FUor sources (e.g., Cieza et al. 2018). Equation 1 can be integrated to calculate the disk mass as:

$$M_d = \frac{2\pi R_c^2 \Sigma_c}{2-\gamma}. \quad (3)$$

This simple disk can therefore be described by 5 free parameters M_d , γ , R_c , H_{100} and Ψ (flaring). The flux emerging from the parametric disk model is computed using the radiative transfer code RADMC-3D (Dullemond et al. 2012). Since FU Ori is a variable embedded object, the information about its stellar spectrum is not well known. Here we assume an effective stellar temperature of 10^4 K and a stellar radius of $5 R_\odot$ to account for the stellar photosphere and the accretion luminosity. The computational grid extends from the radius at which the dust temperature is higher than the sublimation temperature of 1200 K , up to an outer radius of 100 au . Since the model is axisymmetric, the computation is only done in radius and colatitude. The latter extends from 0 (pole) to $\pi/2$ (midplane) radians. Radial and colatitude domains are sampled with a grid of 256 by 64 cells, respectively.

We adopt a distribution of dust grains with a power-law in size a , given by $n(a) \propto a^{-3.5}$, extending from $0.1 \mu\text{m}$ to 3 mm . For the dust optical properties, we use a mix of amorphous carbon grains and astrosilicate grains (see Cieza et al. 2018, for details). The absorption opacity at 1.3 mm is thus $\kappa_{\text{abs}} = 2.2 \text{ cm}^2 \text{g}^{-1}$. The temperature of the dust particles is calculated using RADMC3D's `mtherm` module. Since we aim to explore thousands of different models, the modified random walk option is enabled to speed up calculation over optically thick regions.

The model parameters $\{M_d, \gamma, R_c, H_{100}, \Psi\}$ were constrained using a Bayesian approach. In addition to the disk structure parameters, a centroid shift (δx , δy) is also optimized. The inclination angle i and PA of the model are fixed to the values obtained from `imfit` (see Sec. 2.1). This is a compromise we think necessary as the emission subtends only 2-3 resolution beams. As will be shown in Sec. 4, this disk orientation is consistent with signatures of Keplerian rotation seen in ^{12}CO channel maps.

A 1.3 mm image is produced via ray-tracing, using RADMC3D's second-order integration of the radiative transfer equation. The model visibilities are interpolated to the same uv points as the observations via a Fast Fourier Transform (we use the same algorithm used and described in Cieza

et al. 2018; Marino et al. 2017). These model visibilities are compared against the observed visibilities of each component in FU Ori.

The posterior distributions of each parameter are sampled with the EMCEE MCMC algorithm (Foreman-Mackey et al. 2013). This allows to determine the set of parameters which maximises the likelihood function (via a χ^2 comparison computed on the visibility plane). Since the disk model neglects viscous heating, the derived temperatures serve only as a crude approximation. Nevertheless, it allows for an estimate of the size and bulk mass of the dust disk to be obtained.

3.2. Modeling results

The results of the MCMC radiative transfer modeling, after running 2000 iterations (~ 10 times the autocorrelation time) with 240 walkers, are shown in Fig. 2. The posterior distributions of the disk structural parameters are single peaked and relatively narrow, for both components. The 1.3 mm observations of FU Ori N and FU Ori S can be described by disk profiles, with characteristic radii of approximately 11 au for both disks. The slope of the surface density distribution is ~ 0.5 , also similar for both disks. The northern component requires a slightly hotter disk with a scale-height $H_{100} \approx 2.8$, compared to the southern dust emission which requires a scale-height of $\sim 2.3 \text{ au}$ at 100 au . See corner plots in Fig. 2 for parameter uncertainties.

The masses of the dust disks derived from our best radiative transfer models are relatively small, with $22 \pm 2 M_\oplus$ for FU Ori N and $8.8 \pm 1.4 M_\oplus$ for FU Ori S. Our RT calculations show that the disks around northern and southern components become optically thick at $r \leq 11 \text{ au}$ and $r \leq 6 \text{ au}$, respectively, therefore the inferred total dust masses are likely underestimated.

This can be explained by the temperatures in our RT calculation, which reach higher values than the 20 K assumed in previous works. If the bulk of mass comes from a region at $\sim 50\text{--}80 \text{ K}$, the mass estimates agree within uncertainties.

4. ^{12}CO KINEMATICS

4.1. Evidence of disk rotation around each component

Fig. 3 shows the ^{12}CO channel maps spanning 11 km s^{-1} in velocity, centered near FU Ori N's systemic speed of 11.4 km s^{-1} . The closest channel to systemic velocity (12 km s^{-1}) suffers from foreground absorption. The location of each disk is indicated with white (dashed) crosses, with major axes parallel to the disk PA inferred from the continuum data.

The local kinematics around the location of FU Ori north shows the signature of a rotating disk. The emission changes from blue-shifted (velocities $\leq 11 \text{ km s}^{-1}$, in direction south-east) to red-shifted ($\geq 13 \text{ km s}^{-1}$, towards north-west). The

¹ The systemic velocity of each component was determined via a Gaussian fit to the wings of the line profiles integrated over $0''.15$ apertures centered on each star. The systemic speeds of the northern and southern components are thus 11.4 and 10.1 km s^{-1} , respectively (with uncertainties of about a fifth of the channel width, i.e., 0.2 km s^{-1}).

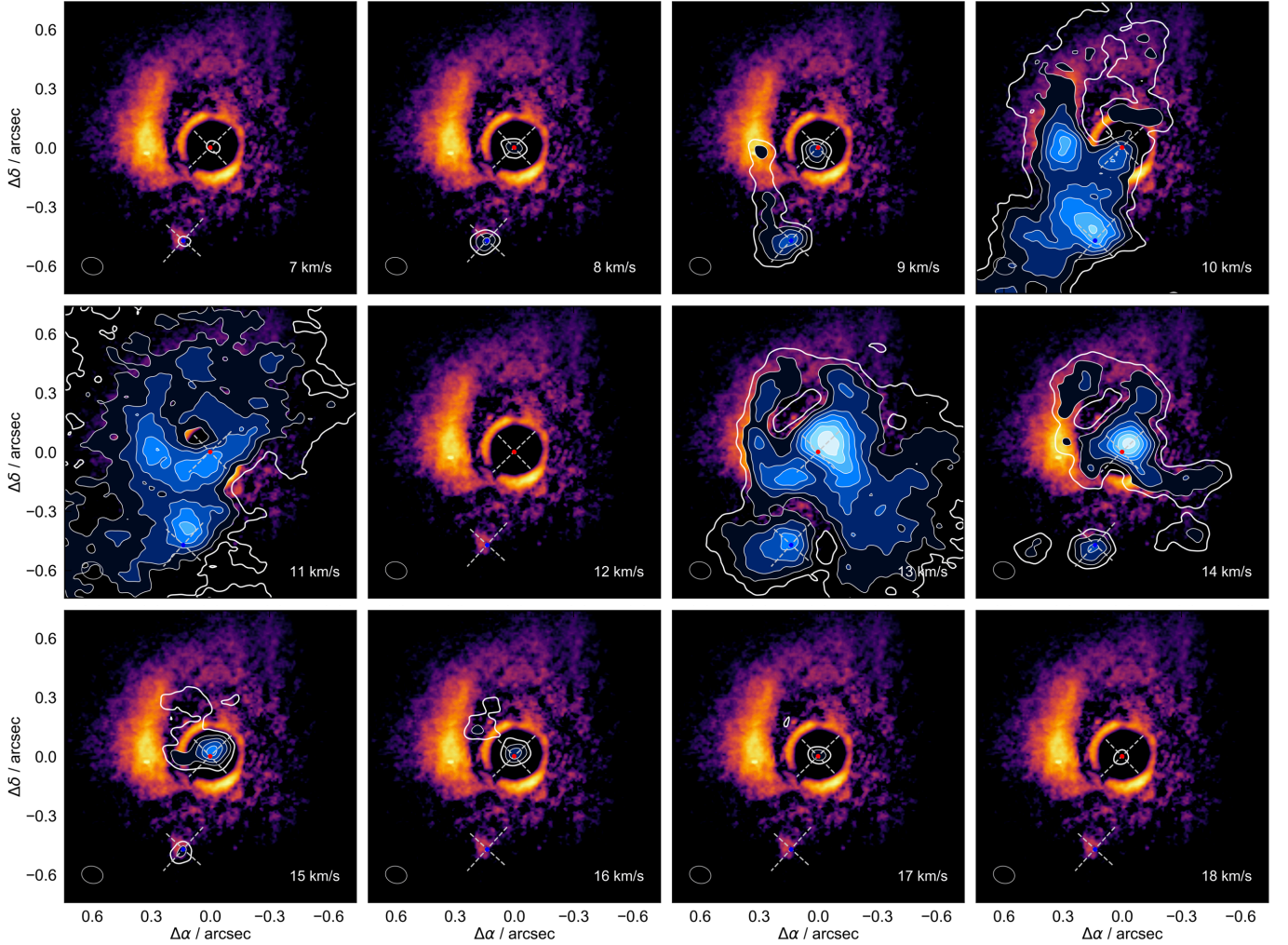


Figure 3. Complex kinematic environment and evidence of disk rotation seen in the ^{12}CO channel maps of the FU Ori system. The orientation (PA and inclination) inferred from the continuum maps are indicated by the white dashed lines for each disk. The northern component shows signatures of rotation as blue- and red-shifted ^{12}CO emission loci along the disk PA. The red and blue points show the stellar locations of FU Ori north and south, respectively. The velocities, in km s^{-1} , are given in the lower right corners. Each panel shows ^{12}CO emission via color-filled contour maps for 13, 17, 21, 25, 29, 33, 37, and 41 mJy beam^{-1} . The thicker unfilled white contour shows the 5σ level, i.e., 10 mJy beam^{-1} (σ is 2 mJy beam^{-1}). The beam size is shown as a grey ellipse in the lower left corner. The systemic velocity ($\sim 11.7 \text{ km s}^{-1}$) channel at 12 km s^{-1} suffers heavy foreground absorption and displays no emission above 5σ . Relative RA and DEC are shown with respect to the location of FU Ori north (peak of the continuum). The background image shows the HiCIAO polarized scattered light map published in Takami et al. (2018), see also Liu et al. (2016).

red- and blue-shifted emission loci are symmetric with respect to the peak in dust continuum, along a disk PA of 135° east of north, i.e., the disk orientation derived from the continuum emission.

Evidence of spatially-resolved disk rotation around FU Ori south is also present in the channel maps, although less clear than the emission patterns in the vicinity of the northern component. There is a switch from blue- to red-shifted emission along the southern continuum disk PA. The switch happens at a systemic speed (for the southern disk) between the 9 and 10 km s^{-1} channels. The southern disk emission is much fainter than its northern counterpart in channels with velocities $> 11 \text{ km s}^{-1}$. This could be due to intra-cloud absorption

around the southern component. The larger scale kinematics is complex and heavily influenced by cloud emission and absorption, and also by a slow outflow (Hales et al. *in prep*).

CO channels show a prominent elongated emission feature between 9 and 14 km s^{-1} , immediately east to the primary. At 9 km s^{-1} , the extended emission is connected (via the lower level flux contour) to the southern component's kinematics. Yet, at 10 and 11 km s^{-1} the emission appears connected to the northern component's blue-shifted disk kinematics. Interestingly, the brightest feature seen in reflected light also appears as an arc-like elongation to the east of FU Ori north (Takami et al. 2018). As shown in Fig. 3, the extended arc in CO emission indeed could be counterpart to the bright arc in

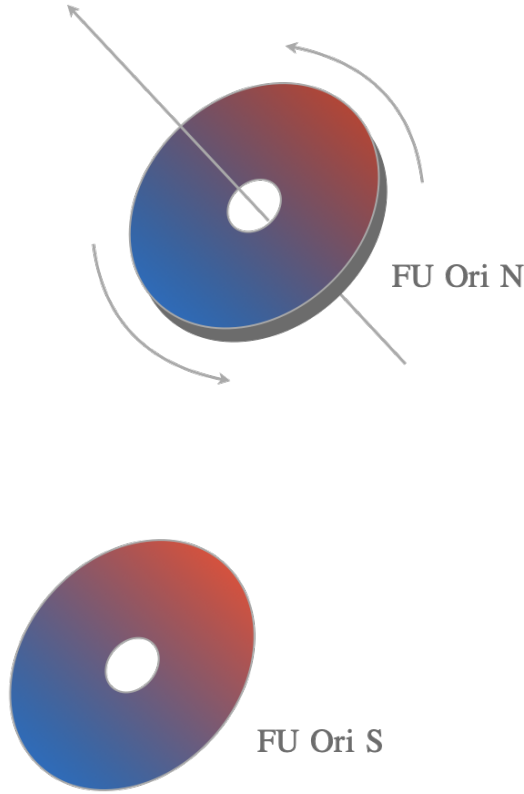


Figure 4. Cartoon representation showing the geometry and the kinematics of the FU Ori system. The disks are scaled up to aid visualization. The inclination and position angles are as inferred from the continuum image. The kinematics (blue/red gradient) is consistent with the ^{12}CO channel maps. The inner holes are drawn for aesthetic reasons.

scattered light. This would imply that the arc-like structure could be moving at (projected) speeds of $\sim 2\text{--}3 \text{ km s}^{-1}$, with respect to the north component's systemic speed.

Although using wide spectral channels allows to pinpoint disk kinematics, this resolution is not ideal to determine the kinematics of the bright blue arc. To study the nature of this feature, whether it is an outflowing or inflowing structure, requires deep gas observations in optically thinner tracers.

The presence of a blue-shifted large scale outflow to the north-east of FU Ori, as well as a red-shifted counterpart to the south-west, will be presented in a future work (Hales et al. *in prep*). Assuming that the outflow is launched from the FU Ori N disk implies that the near side of the disk is to the south-west. The evidence for rotation seen in the ^{12}CO channel maps allows to infer counter-clockwise disk rotation in the plane of the sky. Figure 4 shows a cartoon representation of the inferred geometries of the FU Ori binary. The inclinations and position angles correspond to those calculated from the continuum image. The kinematics of each disk, inferred from the ^{12}CO channel maps, is shown as a red/blue gradient. In the case of FU Ori S, the disk's near/far side and the sense of rotation are unknown.

5. DISCUSSION

5.1. FU Ori disk sizes and masses

Modeling of the continuum emission yields disk sizes that are $\sim 11 \text{ AU}$ in characteristic radius for both components. These small disk sizes are comparable to those of protostellar disks, which have typical radii of less than 10 au at 8 mm (Segura-Cox et al. 2018). The slope of the density distribution of each FU Ori disk is ~ 0.4 , closer to T Tauri disks (Andrews et al. 2010) than other FUor sources observed at 1.3 mm (Cieza et al. 2018). The dust masses and disk sizes inferred from the RT modeling are small compared to the continuum emission from other FUor and EXor sources. Cieza et al. (2018) fit the continuum emission of eight FUor and EXor targets (their figure 6), and found that FUor are more massive than EXor. Interestingly, our resolved observations of FU Ori north and south suggest that the FUor prototype system have dust masses comparable to the EXor sources in Cieza et al. (2018)'s sample.

5.2. Update on the FU Ori accretion disk model

With the assumption that the inclination of FU Ori N is 55° , previous SED fitting to its optical-IR spectrum suggests that FU Ori N harbors a disk accreting at a rate of $\dot{M} \approx 2.4 \times 10^{-4} \text{ M}_\odot \text{ yr}^{-1}$ around a 0.3 M_\odot star (Zhu et al. 2007). The inner radius is 5 R_\odot in this accretion disk model. Our observations presented here suggest an inclination angle of $\sim 35^\circ$. This new inclination allows us to update the disk and star parameters for FU Ori N. First, to produce the same line-width that explains the optical spectrum of FU Ori (Zhu et al. 2009), the stellar mass has to increase to 0.6 M_\odot . With the smaller inclination angle, the disk luminosity is only 70% of the previous estimate, which leads to 84% of the previous disk inner radius and 59% of the previous \dot{M} value. Thus, the disk inner radius is 3.5 R_\odot and \dot{M} is $3.8 \times 10^{-5} \text{ M}_\odot \text{ yr}^{-1}$ with the new central star mass.

Given the very low mass of the disks and the high accretion rate inferred above, the accretion event must last for a short time compared to the disk lifetime. The high accretion rate suggests that the mechanism behind the outbursts in luminosity happens in an episodic way. There is the possibility that the disk mass is replenished efficiently by inflow of material from the cloud or by cloudlet capture (e.g., Dullemond et al. 2019). Our observations do not rule out the presence of inflowing material and we hope to further explore this scenario in follow-up observations connecting the large scale outflows with higher sensitivity and resolution local kinematics. In the following section we discuss the possibility of interaction scenarios.

5.3. Dynamically perturbed kinematics?

The disk rotation pattern around both components are skewed, in the sense that a unique PA is not sufficient to represent the emission loci over the full velocity range. In the FU Ori binary system, this could suggest that the disks are being perturbed by mutual interactions. An internal perturbation, e.g. driven by self-gravity, is unlikely given the

low mass of the disks. Given the proximity of both stars, we think that gravitational interactions are likely to be at play. Although the dust disks share similar geometries, the orbit of the perturber, FU Ori south, need not be in the same plane. The bright arc, seen in scattered light and CO in Fig. 3 may be explained as a dynamical feature out of the plane of the FU Ori north disk if created by flyby or disk-disk encounter (see Cuello et al. 2019, , their fig. 4).

The compact size of the dust disks can also be explained within a flyby scenario. An (inclined) prograde encounter, besides stripping the disk of dust material in the outer regions, leads to an enhancement of the density in the inner regions of the disk (see red curves in Cuello et al. 2019, their figure 11). This prograde encounter could also potentially explain the outburst event via enhanced accretion. However, in this case the perturbation only happens once.

An alternative scenario to a disk-disk interaction has been proposed by Dullemond et al. (2019). Here, the capture of a cloudlet or cloud fragment also leads to arc-shaped reflection nebulae. The capture of this cloud fragment also replenishes the disk allowing for a fresh supply of material to maintain the high accretion rate.

6. CONCLUDING REMARKS

The new 1.3 mm ALMA data presented here resolve the continuum and gas emission around both FU Ori components. We have derived sizes and orientations for each disk from continuum emission. The disk orientations suggest that FU Ori north and south share similar inclination angles. If we were to assume the disk are in near coplanar configuration, they are separated by a deprojected distance of 250 au. Their sizes are remarkably similar taking into account that the southern stellar component is at least twice as massive as the northern star (Beck & Aspin 2012).

The spatially-resolved ^{12}CO kinematics allowed for disk rotation to be identified in the vicinity of each component. The emission revealing disk rotation also appears asymmetric and skewed, suggesting the disks are subject to interaction in the form of a flyby. This interaction could be due to a mutual disk-disk encounter and/or cloudlet capture within the cloud. Moreover, the slow channels (near systemic velocity) reveal CO emission which is spatially coincident with the bright reflection arc previously reported in scattered light observations. The elongated feature is, to some extent, connected to both the north and south components. To understand whether this emission corresponds to inflow or outflow to or from any of the FU Ori components will require deeper CO observations to sample the kinematics with finer spec-

tral resolution and higher sensitivity. The gas observations also show that the systemic speeds of FU Ori north and south differ by at least 1 km s^{-1} , which could inform future dynamical models of the binary interaction. Several FUor type objects have known binary companions, thus investigating the kinematics around these multiple systems can help connect binary interaction and flybys with accretion bursts triggers.

The disks in FU Ori north and south are compact and mostly optically thick, even at mm wavelengths (similarly to Class I, Sheehan & Eisner 2017; Segura-Cox et al. 2018). In order to determine the disk masses and dust properties within these central regions, observations at longer wavelengths with AU-scale resolutions will be required (i.e., at next-generation Very Large Array baselines, White et al. 2018; Murphy et al. 2018).

We thank the anonymous referee for a constructive report. We also thank Sebastián Marino for providing the tool to sample the model in visibilities, Ed Fomalont for useful discussions and suggestions during the analysis of the data, and Michihiro Takami and Jun Hashimoto for providing the HiCIAO image, as well as useful comments. SP acknowledges support from CONICYT-Gemini grant 32130007, CONICYT-Fondecyt Regular grants 1191934, and the Joint Committee of ESO and the Government of Chile. H.B.L. is supported by the Ministry of Science and Technology (MoST) of Taiwan (Grant Nos. 108-2112-M-001-002-MY3 and 108-2923-M-001-006-MY3). NC acknowledges financial support provided by FONDECYT grant 3170680. We acknowledge support from the Millennium Science Initiative (Chile) through grant RC130007. This work used the Breka cluster, financed by Fondecyt project EQM140101, hosted at DAS/U. de Chile. This paper makes use of the following ALMA data: ADS/JAO.ALMA.2016.1.01228.S. ALMA is a partnership of ESO (representing its member states), NSF (USA) and NINS (Japan), together with NRC (Canada) and NSC and ASIAA (Taiwan), in cooperation with the Republic of Chile. The Joint ALMA Observatory is operated by ESO, AUI/NRAO and NAOJ. The National Radio Astronomy Observatory is a facility of the National Science Foundation operated under cooperative agreement by Associated Universities, Inc.

Facility: ALMA.

Software: emcee (Foreman-Mackey et al. 2013), radmc-3d (Dullemond et al. 2012), Common Astronomy Software Applications (McMullin et al. 2007), astropy (Astropy Collaboration et al. 2013)

REFERENCES

- Andrews, S. M., Wilner, D. J., Hughes, A. M., Qi, C., & Dullemond, C. P. 2010, *ApJ*, 723, 1241
- Armitage, P. J., Livio, M., & Pringle, J. E. 2001, *MNRAS*, 324, 705
- Astropy Collaboration, Robitaille, T. P., Tollerud, E. J., et al. 2013, *A&A*, 558, A33
- ALMA Partnership, Brogan, C. L., Pérez, L. M., et al. 2015, *ApJL*, 808, L3
- Audard, M., Ábrahám, P., Dunham, M. M., et al. 2014, *Protostars and Planets VI*, 387
- Bae, J., Hartmann, L., Zhu, Z., & Nelson, R. P. 2014, *ApJ*, 795, 61

- Beck, T. L., & Aspin, C. 2012, *AJ*, 143, 55
- Beckwith, S. V. W., Sargent, A. I., Chini, R. S., & Guesten, R. 1990, *AJ*, 99, 924
- Bonnell, I., & Bastien, P. 1992, *ApJL*, 401, L31
- Cieza, L. A., Casassus, S., Tobin, J., et al. 2016, *Nature*, 535, 258
- Cieza, L. A., Ruíz-Rodríguez, D., Perez, S., et al. 2018, *MNRAS*, 474, 4347
- Clarke, C., Lodato, G., Melnikov, S. Y., et al. 2005, *MNRAS*, 361, 942
- Cuello, N., Dipierro, G., Mentiplay, D., et al. 2019, *MNRAS*, 483, 4114
- Cuello, N., Louvet, F., Mentiplay, D., et al. 2019, *MNRAS*, 2545
- Dullemond, C. P., Juhasz, A., Pohl, A., et al. 2012, *Astrophysics Source Code Library*, ascl:1202.015
- Dullemond, C. P., Küffmeier, M., Goicovic, F., et al. 2019, *A&A*, 628, A20
- Evans, N. J., II, Dunham, M. M., Jørgensen, J. K., et al. 2009, *ApJS*, 181, 321-350
- Foreman-Mackey, D., Hogg, D. W., Lang, D., & Goodman, J. 2013, *PASP*, 125, 306
- Foreman-Mackey, D. 2016, *The Journal of Open Source Software*, 1,
- Gaia Collaboration, Brown, A. G. A., Vallenari, A., et al. 2018, *A&A*, 616, A1
- Hales, A. S., Corder, S. A., Dent, W. R. D., et al. 2015, *ApJ*, 812, 134
- Hales, A. S., Pérez, S., Saito, M., et al. 2018, *ApJ*, 859, 111
- Hildebrand, R. H. 1983, *QJRAS*, 24, 267
- Kenyon, S. J., Hartmann, L. W., Strom, K. M., & Strom, S. E. 1990, *AJ*, 99, 869
- Keto, E. 2003, *ApJ*, 599, 1196
- Li, J. I., Liu, H. B., Hasegawa, Y., & Hirano, N. 2017, *ApJ*, 840, 72
- Liu, H. B., Takami, M., Kudo, T., et al. 2016, *Science Advances*, 2, e1500875
- Liu, H. B., Vorobyov, E. I., Dong, R., et al. 2017, *A&A*, 602, A19
- Liu, H. B., Dunham, M. M., Pascucci, I., et al. 2018, *A&A*, 612, A54
- Liu, H. B., Mérand, A., Green, J. D., et al. 2019, *ApJ*, 884, 97
- Marino, S., Wyatt, M. C., Panić, O., et al. 2017, *MNRAS*, 465, 2595
- Martin, R. G., & Lubow, S. H. 2011, *ApJL*, 740, L6
- Menten, K. M., Reid, M. J., Forbrich, J., & Brunthaler, A. 2007, *A&A*, 474, 515
- Mezger, P. G., & Henderson, A. P. 1967, *ApJ*, 147, 471
- McMullin, J. P., Waters, B., Schiebel, D., Young, W., & Golap, K. 2007, *Astronomical Data Analysis Software and Systems XVI*, 376, 127
- Muñoz, D. J., Kratter, K., Vogelsberger, M., Hernquist, L., & Springel, V. 2015, *MNRAS*, 446, 2010
- Murphy, E. J., Bolatto, A., Chatterjee, S., et al. 2018, *Science with a Next Generation Very Large Array*, 3.
- Pueyo, L., Hillenbrand, L., Vasisht, G., et al. 2012, *ApJ*, 757, 57
- Pfalzner, S. 2008, *A&A*, 492, 735.
- Principe, D. A., Cieza, L., Hales, A., et al. 2018, *MNRAS*, 473, 879.
- Reipurth, B., & Aspin, C. 2004, *ApJL*, 608, L65
- Ruíz-Rodríguez, D., Cieza, L. A., Williams, J. P., et al. 2017, *MNRAS*, 468, 3266.
- Ruíz-Rodríguez, D., Cieza, L. A., Williams, J. P., et al. 2017, *MNRAS*, 466, 3519.
- Segura-Cox, D. M., Looney, L. W., Tobin, J. J., et al. 2018, *ApJ*, 866, 161.
- Sheehan, P. D., & Eisner, J. A. 2017, *ApJ*, 851, 45.
- Takami, M., Fu, G., Liu, H. B., et al. 2018, *ApJ*, 864, 20.
- Tobin, J., Sheehan, P., & Johnstone, D. 2018, *arXiv e-prints*, arXiv:1810.06590.
- Vorobyov, E. I., & Basu, S. 2010, *ApJ*, 719, 1896
- Walsh, C., Millar, T. J., & Nomura, H. 2010, *ApJ*, 722, 1607
- White, J. A., Audard, M., Ábrahám, P., et al. 2018, *Science with a Next Generation Very Large Array*, 177.
- Wilson, T. L., Rohlfs, K., & Hüttemeister, S. 2009, *Tools of Radio Astronomy*, by Thomas L. Wilson; Kristen Rohlfs and Susanne Hüttemeister. ISBN 978-3-540-85121-9. Published by Springer-Verlag, Berlin, Germany, 2009.,
- Zhu, Z., Hartmann, L., Calvet, N., et al. 2007, *ApJ*, 669, 483.
- Zhu, Z., Hartmann, L., Gammie, C., & McKinney, J. C. 2009, *ApJ*, 701, 620
- Zhu, Z., Espaillat, C., Hinkle, K., et al. 2009, *ApJL*, 694, L64
- Zhu, Z., Hartmann, L., Gammie, C. F., et al. 2010, *ApJ*, 713, 1134
- Zurlo, A., Cieza, L. A., Williams, J. P., et al. 2017, *MNRAS*, 465, 834.